ELSEVIER

Contents lists available at ScienceDirect

Materials Characterization

journal homepage: www.elsevier.com/locate/matchar



Influence of severe plastic deformation on the microstructure and hardness of a CoCrFeNi high-entropy alloy: A comparison with CoCrFeNiMn



Jenő Gubicza^{a,*}, Pham Tran Hung^a, Megumi Kawasaki^b, Jae-Kyung Han^b, Yakai Zhao^c, Yunfei Xue^c, János L. Lábár^{a,d}

- ^a Department of Materials Physics, Eötvös Loránd University, Budapest, P.O.B. 32, H-1518, Hungary
- ^b School of Mechanical, Industrial and Manufacturing Engineering, Oregon State University, Corvallis, OR 97331, USA
- ^c School of Materials Science and Engineering, Beijing Institute of Technology, Beijing 100081, China
- d Institute for Technical Physics and Materials Science, Centre for Energy Research, Hungarian Academy of Sciences, Budapest, Hungary

ARTICLE INFO

Keywords: High-entropy alloys Severe plastic deformation Microstructure Dislocations Twin faults Hardness

ABSTRACT

The evolution of microstructure and hardness in a CoCrFeNi high-entropy alloy (HEA) processed by severe plastic deformation (SPD) was studied. SPD-processing was carried out using a high-pressure torsion (HPT) technique up to twenty turns at room temperature that introduces a highest nominal shear strain of about 800. It was found that most of grain refinement and an increase of lattice defect (dislocations and twin faults) density occurred up to the shear strain of \sim 10. The saturation grain size was about 80 nm, while the maximum values of the dislocation density and the twin fault probability were \sim 150 \times 10¹⁴ m⁻² and \sim 3%, respectively. In addition, a 111 texture was formed during HPT-processing. The evolution of hardness with strain followed a trend suggested by the changes in the microstructure. The saturation hardness was as high as \sim 5100 MPa. The microstructure and hardness obtained for the HPT-processed CoCrFeNi were compared with the values determined formerly for CoCrFeNiMn. It was found that, although the saturation grain size in the CoCrFeNi was much higher than that for the CoCrFeNiMn HEA, the hardness was similar for the two alloys due to the close values of the twin fault probability which can be explained by the similar stacking fault energies.

1. Introduction

In recent years, high-entropy alloys (HEAs) have received increasing attention from the scientific community. Unlike conventional alloys, where only one principle element is used in the matrix with a limited addition of other elements for property enhancement, these newly-developed alloys are designed to have multiple principle elements with equal or nearly equal atomic ratios [1]. Even though having been intensively studied both theoretically and experimentally, HEAs with their intricate structure open further questions, evidently with an exponential increase in numbers of related articles [2]. HEAs exhibit excellent and unique mechanical properties, such as high fatigue and wear resistance even at elevated temperatures (e.g., for VNbMoTaW), or high hardness and good friction resistance even in body fluids (e.g., for TiZrNbHfTa)N and (TiZrNbHfTa)C alloys) [3]. Since lattices of HEAs are strongly distorted, dislocation motion is restricted, which helps to increase the strength of these materials [4]. One of the key features of HEAs is having a high-entropy configuration, resulting in a single-phase solid solution at room temperature. However, in contrast

to the vast number of possible HEA compositions, the variety of singlephase solid solution HEAs produced from conventional ingot metallurgy processing is rather limited, e.g., due to the low thermal stability [5]. For example, the mostly studied HEA of CoCrMnFeNi is unstable when prolongedly exposed to an intermediate temperature [6]. Vaidya et al. showed that the value of ϕS (the product of thermodynamic factor ϕ and the cross correlation term S) for CoCrMnFeNi is between 3 and 5, implying a deviation from an ideal solid solution, while CoCrFeNi has a value close to unity for ϕS , suggesting the material to be an ideal solid solution [7]. Moreover, Huo et al. presented that CoCrFeNi produced by arc melting meets the criteria to form simple solid solutions [8]. In addition, CoCrFeNi is an attractive HEA as a base material of various HEAs for mechanical improvements. For instance, an addition of Cu to CoCrFeNi decreased its wear rate [9], and an addition of Mn increased its grain growth resistance [10]. Thus, the present study focuses on a CoCrFeNi HEA material.

Beside the addition of new elements for HEAs, tailoring of the microstructure is another way for improving the mechanical properties of HEAs. For example, a cold drawn CoCrFeNi wire yielded a strength as

E-mail address: jeno.gubicza@ttk.elte.hu (J. Gubicza).

^{*} Corresponding author.

high as 1.1 GPa at 293 K and 0.8 GPa at 923 K due to the refined microstructure [11]. A nano-twinned nanocrystalline CoCrFeNi produced by magnetron sputtering exhibited a hardness of about 9 GPa [12]. Precipitates and contamination formed during material processing may also result in an enhanced yield strength of CoCrFeNi HEAs [13-15]. Another attractive way to improve the strength of CoCrFeNi alloys is grain refinement [16], as the formed lattice defects serve as obstacles to dislocation motion. One of the most powerful approaches to achieve ultrafine-grained (UFG) or nanocrystalline materials without any contamination or porosity is through severe plastic deformation (SPD) [5]. Among SPD techniques, high-pressure torsion (HPT) processing can vield exceptional grain refinement and strength improvement [17]. For instance, for an Al_{0.3}CoCrFeNi HPT-processing and subsequent annealing led to a fourfold increase of hardness and an additional homogenization of elemental distribution [18]. Moreover, a CoCr-FeMnNi processed by HPT yielded four times higher hardness compared to the unprocessed material [4]. Although, HPT is expected to lead to an improvement in the strength of a bulk CoCrFeNi, this effect has not been studied yet in detail. An investigation of the evolution in the density of lattice defects, such as dislocations and twin faults, during HPT on a CoCrFeNi HEA is also missing in the literature. This study aims to fill this gap. In addition, a comparison between the microstructures and hardness values of the HPT-processed CoCrFeNi and CoCrFeMnNi HEAs will be made.

The aim of this study is to investigate the microstructure and hardness of an equimolar CoCrFeNi HEA processed by HPT. The evolution of microstructure with shear strain is studied after ½, 1, 10 and 20 HPT turns. Electron backscatter diffraction (EBSD) and transmission electron microscopy (TEM) were used to evaluate the grain refinement due to SPD-processing. The evolution of lattice defects structure (dislocations and twin faults) was investigated by X-ray line profile analysis (XLPA). The hardness was measured along the disk radius and its relation to the microstructure was studied as a function of shear strain. Moreover, the grain size, the defect densities and the hardness obtained for the CoCrFeNi HEA were compared to the values determined for an HPT-processed CoCrFeNiMn alloy in order to reveal the differences in microstructure evolution and mechanical properties as well as the possible deformation mechanisms.

2. Material and methods

2.1. Processing of the material

The $Co_{25}Cr_{25}Fe_{25}Ni_{25}$ HEA samples were prepared by vacuum induction melting and drop casting of a mixture of pure metals (purity > 99.9 wt%). The cast ingot with a thickness of ~39 mm was hot-rolled at $1050\,^{\circ}C$ to a thickness of ~14 mm which corresponds to a thickness reduction of ~64%. Then, the hot-rolled plate was homogenized at $1100\,^{\circ}C$ for 1 h. This material was machined into billets with a diameter of 10 mm which were sliced by electric discharge machining (EDM) to have a final thickness of ~0.85 mm. Processing by HPT was conducted by utilizing the conventional HPT facility with quasi-constrained set-up [19]. The processing was operated at room temperature under 6.0 GPa at 1 rpm for $\frac{1}{2}$, 1, 10 and 20 turns.

2.2. Microstructure studied by electron microscopy

The microstructure in the initial sample as well as in the centers of the disks processed by ¼ and 1 turn was investigated by EBSD. In the centers of the disks processed by 10 and 20 turns and at the peripheries for all HPT samples, TEM was used for the study of the microstructure since the small grain size and the severely deformed crystal lattice inhibit the adequate microstructural examination by EBSD. The EBSD examination was carried out using an FEI Quanta 3D scanning electron microscope (SEM). The sample surfaces for EBSD were first mechanically polished with 1200, 2500 and 4000 grit SiC abrasive papers, and

then the polishing was continued with a colloidal alumina suspension with a particle size of $1\,\mu m.$ In the final step of mechanical polishing, the samples were polished with a colloidal silica suspension (OP-S) with a particle size of 40 nm. Finally, the surfaces were electropolished at 25 V and 1 A using an electrolyte with a composition of 70% ethanol, 20% glycerine and 10% perchloric acid (in vol%). The step sizes in the EBSD images were 400 and 140 nm for the initial and HPT-processed samples, respectively. The EBSD images were evaluated using the Orientation Imaging Microscopy (OIM) software. The same SEM facility was used for the energy-dispersive X-ray spectroscopy (EDS) measurement of the spatial distributions of the chemical elements.

For the TEM characterization, thin TEM-lamellae were prepared from pieces of bulk samples by Ar-ion milling with taking special care to avoid heating leading to microstructural changes and possible phase transformation of the samples during preparation. First, the samples were glued to a Cu-stub for mechanical grinding and polishing using special glue at 100 °C for not > 1 min. Second, ion-beam thinning of the $50\,\mu m$ thick lamella was started at 7 keV using $2\,mA$ ion-current. The samples were cooled with liquid nitrogen during thinning. Finally, the perforated lamella was cleaned at 3 keV and later at 1 keV from both sides to remove damaged layers from its surfaces. TEM bright-field (BF) and dark-field (DF) images were recorded in a Titan Themis G2 200 transmission electron microscope. The TEM images were recorded at 200 keV with a 4 k*4 k CETA 16 CMOS camera controlled by VELOX software. The number of grains analyzed in the TEM images for each sample was about 50. The uncertainty of the average grain size values was about 10%.

2.3. Microstructure characterization by X-ray diffraction

The crystal structure of the CoCrFeNi samples was studied with X-ray diffraction (XRD), using a Philips Xpert powder diffractometer with CuK α radiation (wavelength: 0.15418 nm) and a secondary graphite monochromator. The resulted X-ray diffractograms showed that all samples have a single phase face-centered cubic (fcc) structure. The average lattice constant was determined for the whole surfaces of the HPT-processed disks from the diffraction peak positions using the Nelson-Riley method [20].

The lattice defect structure was investigated locally at the centers and the peripheries of the HPT-processed samples by applying XLPA, using an X-ray diffractometer operating at 30 kV and 25 mA with CoKα₁ radiation (wavelength: 0.1789 nm) and a single crystal Ge monochromator. In these experiments, the Debye-Scherrer diffraction rings were measured by two-dimensional imaging plates. The X-ray line profiles obtained from the Debye-Scherrer rings were evaluated with the Convolutional Multiple Whole Profile (CMWP) fitting method [21]. In this procedure, all measured diffraction peaks were fitted with the convolution of theoretical microstructural profiles related to diffraction domain size, dislocation density and twin faults. The diffraction peak broadening caused by dislocations depends on the indices of reflections and it is taken into account by the dislocation contrast factors [21]. The knowledge of these contrast factors is necessary for the determination of the dislocation density by the XLPA method. The dislocation contrast factors for the CoCrFeNi HEA were determined by the software ANIZC [22] using the elastic constants $c_{11} = 271 \text{ GPa}$, $c_{12} = 175 \text{ GPa}$ and $c_{44} = 189 \,\text{GPa}$ [23]. The average contrast factors for cubic crystals depend on two parameters denoted as \overline{C}_{h00} and q. The values of q were 1.72 and 2.49 for edge and screw dislocations, respectively, for CoCr-FeNi as determined by ANIZC while \overline{C}_{h00} were 0.31 and 0.33 for edge and screw dislocations, respectively. The CMWP method yields the median (m) and the lognormal variance (σ) of the assumed lognormal size distribution, the dislocation density and the twin fault probability with good statistics. The area-weighted mean diffraction domain size was determined from m and σ as $m \times exp(2.5\sigma^2)$. The twin fault probability for fcc materials gives the fraction of {111} planes containing twin faults in percentage. Further details of the CMWP method

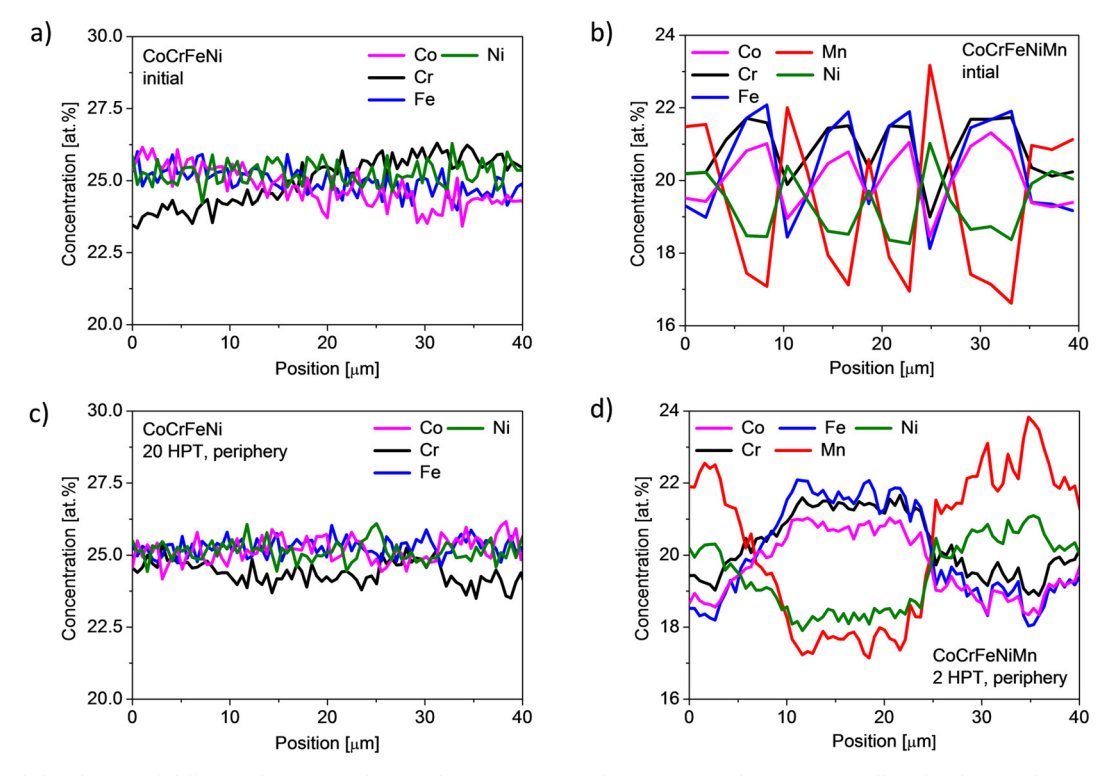


Fig. 1. The spatial distribution of different elements in the initial CoCrFeNi (a) and CoCrFeNiMn (b) HEAs, as well as for the samples processed by HPT till microstructural saturation (c and d). The precision of the concentration values was \pm 1 at.%.

can be found in Ref. [21].

In the present XLPA evaluation, instrumental correction was not applied since the breadth of the measured profiles was one order of magnitude higher than the width of the instrumental peaks measured on a LaB6 standard material. It should be noted, however, that the chemical heterogeneities in HEAs may also result in XRD peak broadening as it was shown for a CoCrFeNiMn alloy in a former study [4]. For that HEA, considerable spatial fluctuations in the element concentrations were detected by EDS which resulted in significantly higher XRD peak broadening for the initial undeformed material than that for the LaB₆ standard sample. Then, this extra broadening was taken into account as increased instrumental broadening when the XRD patterns of the HPT-processed samples were evaluated. In the meanwhile, for the present CoCrFeNi HEA the concentration inhomogeneities were negligible both before and after HPT-processing as shown in Fig. 1a and c, respectively, in comparison with the CoCrFeNiMn before and after HPT as shown in Fig. 1b and d, respectively. Specifically, these spatial distributions of constituents were determined by EDS in the initial states and at the periphery of the disk processed for the highest applied numbers of turns. In the CoCrFeNiMn HEA obtained formerly by solidification (as-cast state) [4], Mn enrichment was detected in the interdendritic regions. In contrast, dendritic microstructure and the corresponding chemical inhomogeneities were not observed in the present CoCrFeNi HEA, since the applied thermomechanical processing (casting + hot-rolling + homogenization) effectively broke the dendrite structure originated from the casting process. Therefore, the effect of chemical heterogeneities was not considered in the evaluation of the XRD line profiles for the present CoCrFeNi HEA.

The size of the X-ray beam spot was about $0.2 \times 2 \, \text{mm}^2$, therefore the defect density values must be interpreted as the average values in these spots. The higher the dislocation density and the twin fault probability in the probed volume, the larger the breadth of the profiles, leading to a more reliable evaluation of the profiles. Thus, the high dislocation densities and twin fault probabilities (i.e., low twin fault spacings) developed in the HPT-processed samples can be determined

by the XLPA method with a high precision. It should be noted that due to the 2 mm height of the X-ray beam spot the results obtained at the disk centers must be interpreted as the average values characterizing the centers of the samples with a radius of 1 mm. The measurement at the periphery was obtained at 4 mm from the disk center.

The crystallographic textures of the initial sample and the HPT-processed disks were characterized by the pole figure measurements using a Smartlab X-ray diffractometer (manufacturer: Rigaku, Japan) with CuK α radiation (wavelength: 0.15418 nm) and parallel-beam optics. In these experiments, the whole disks were irradiated by X-rays, therefore the results characterize the entire sample surface planes.

2.4. Measurement of the hardness

The hardness was determined along the diameters of the disks. The spacing between the neighboring indents was 0.5 mm. The hardness test was performed by a Zwick Roell ZH μ Vickers indenter using a load of 500 g and a dwell time of 10 s.

3. Results

3.1. Evolution of grain size during HPT-processing

The XRD experiments revealed that both the initial sample and the HPT-processed disks are single phase fcc structures with a lattice parameter of 0.3572 \pm 0.0007 nm. Fig. 2a and b shows crystallographic orientation and grain maps, respectively, obtained for the initial material by EBSD. In the grain map, the grains bounded by high-angle grain boundaries (HAGBs) are indicated by different colors. The HAGBs separate volumes with misorientation higher than 15°. The number-weighted average grain size was $\sim\!22\,\mu\text{m}$. The grain boundary misorientation distribution for the initial sample is shown in Fig. 2c. The fraction of HAGBs was 91% with a very high contribution of twin boundaries (about 55%) as suggested by the peak of Σ 3 boundaries in the misorientation distribution at an angle of 60°. The twin boundaries

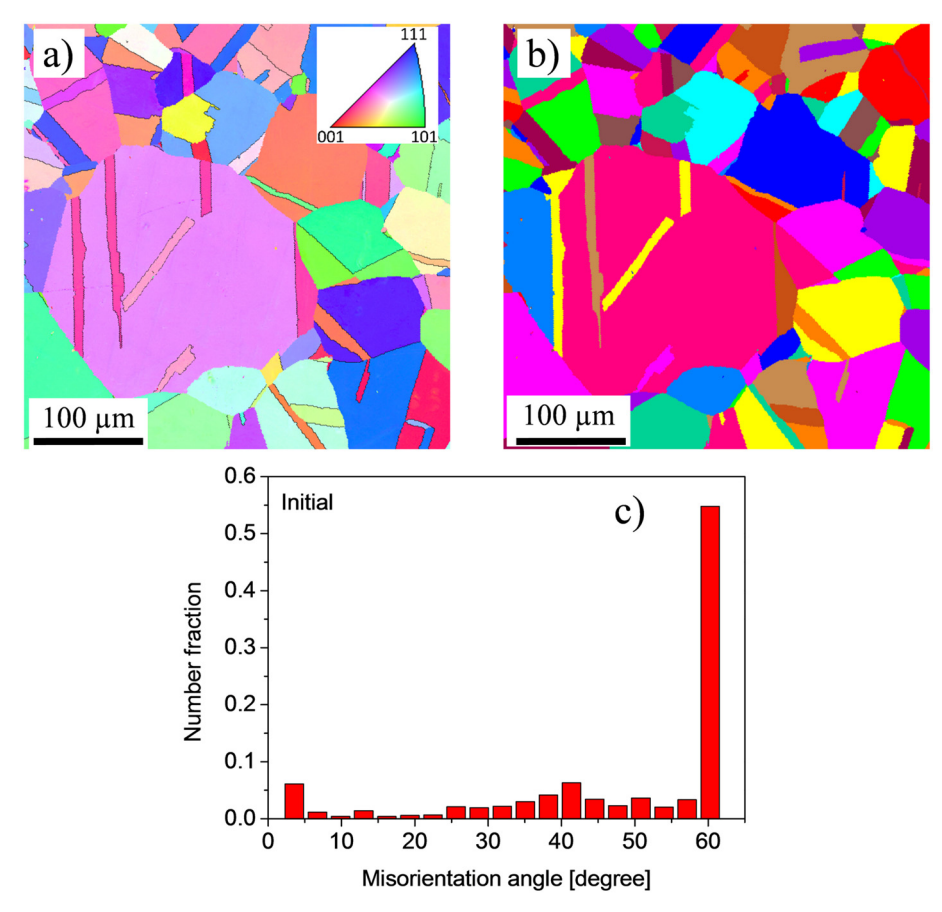


Fig. 2. Orientation (a) and grain (b) maps as well as the misorientation angle distribution (c) for the initial CoCrFeNi HEA.

are indicated by black lines in Fig. 2a.

HPT-processing for 1/4 turn resulted in a significant grain refinement even in the center of the disk as illustrated with the EBSD orientation and grain maps in Fig. 3a and b, respectively. The average grain size in the disk center after $\frac{1}{4}$ turn was ~1.4 µm. Mainly, the original grains were fragmented into lamellas with the formation of many twin boundaries. The significant role of deformation twinning during SPD can be explained by the low SFE of CoCrFeNi HEA (20 mJ/m²) [24]. The formation of a large amount of twin lamellas is apparently in contradiction to the decrease of the $\Sigma 3$ boundary fraction as shown in Fig. 3c. In fact, although the amount of Σ 3 boundaries increased, this trend was overwhelmed by the significant amount of LAGBs (compare Figs. 2c and 3c). Indeed, the fraction of LAGBs in the disk center increased from 9% to 64% during 1/4 turn of HPT which was most probably caused by the formation of a high density of dislocations and their arrangement into LAGBs. The shear deformation caused by dislocation activity may result in the curved shape of twins (see Fig. 3a). It is worth noting that the average grain size determined by the OIM software $(\sim 1.4 \,\mu\text{m})$ seems to be much smaller than the grain size suggested by the EBSD image. This apparent contradiction is caused by two reasons: i) the large number of very small grains with the size of about or < 1 μm and ii) the fact that the number-weighted average grain size was used in the present study. The area-weighted mean grain size given by the OIM software was $\sim 40 \, \mu m$ which is in accordance with the impression suggested by the EBSD image. This effect was caused by the fact that the majority of the image area was occupied by large grains.

Fig. 4a shows an EBSD orientation map for the center of the disk processed for 1 turn by HPT. The corresponding grain map is shown in Fig. 4b. The average grain size was determined as ${\sim}860$ nm. The grain boundary misorientation distribution plotted in Fig. 4c reveals that the $\Sigma3$ boundary fraction in the disk center further decreased from 23% to

9% with increasing number of HPT turns from $\frac{1}{4}$ to one, respectively, while the fraction of LAGBs increased to 69% in the center of the disk after one turn by HPT.

The grain sizes were very small in the centers of the disks processed by 10 and 20 turns of HPT, and therefore TEM was used for the characterization of the grain structure. For comparison purposes, TEM images were also taken for the centers of the samples deformed by 1/4 and 1 turn. Fig. 5 shows sets of a bright-field and the corresponding dark-field TEM images obtained at the disk centers after HPT from 1/4 to 20 turns. Fig. 5b reveals that in the center of the disk processed for 1/4 turn there are twin lamellas with the thicknesses of 100-200 nm (some of them are indicated by white arrows) which cannot be resolved in the EBSD images in Fig. 3. The contrast changes in the TEM images for 1/4 and 1 turn in Fig. 5a-d suggest large defect density even in the centers of the disks. Fig. 5e-h shows that after 10 and 20 turns of HPT a nanocrystalline microstructure was formed in the centers of the disks. The grain sizes determined by microscopic methods are listed in Table 1. The grain size for the center of disk processed by 10 turns was about 80 nm which was maintained reasonably constant through 20 turns.

Fig. 6 shows bright- and dark-field TEM images for the peripheries of the disks processed by $\frac{1}{4}$ turn (a-b), 1 turn (c-d), 10 turns (e-f) and 20 turns (g-h) of HPT. Significant grain refinement was observed in the early stage of HPT for $\frac{1}{4}$ turn and the nanostructure tends to be saturated so that there was no apparent change in the microstructure through 20 HPT turns at the disk edges. In practice, the grain sizes of the processed HEA are measured within the range of 60–90 nm up to 20 HPT turns as shown in Table 1.

3.2. Characterization of microstructure by XLPA

Fig. 7 illustrates the CMWP fitting procedure for the evaluation of

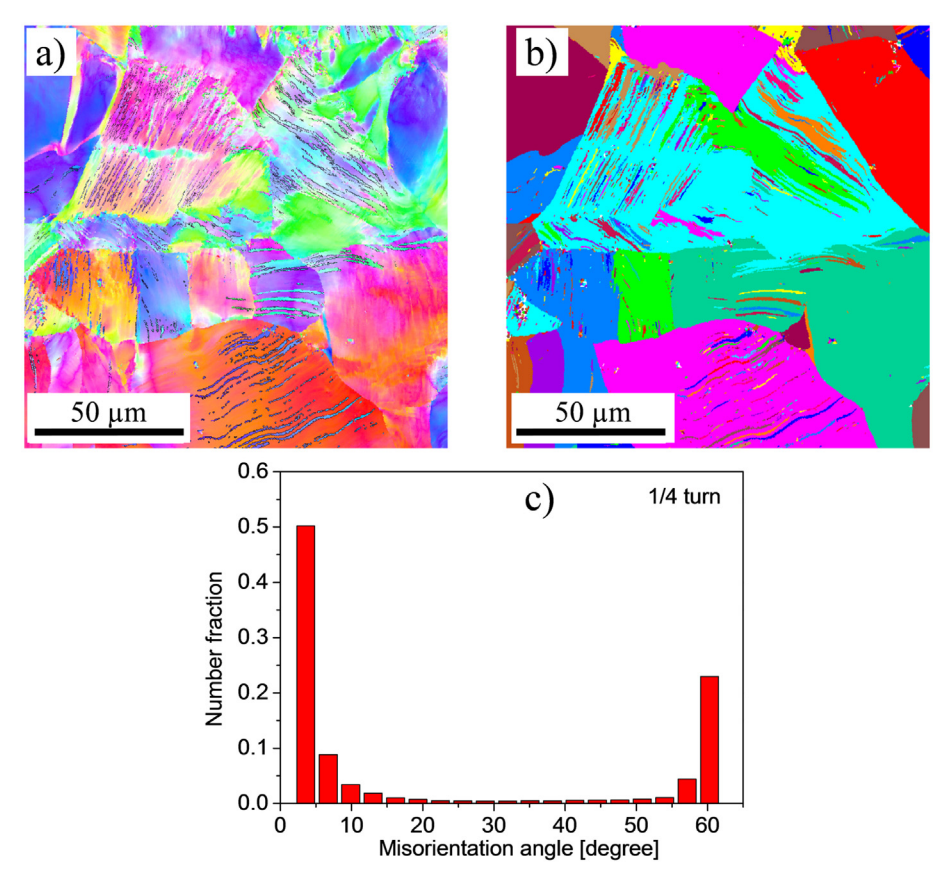


Fig. 3. Orientation (a) and grain (b) maps as well as the misorientation angle distribution (c) for the CoCrFeNi HEA processed by ¼ turn of HPT.

the X-ray line profiles. Namely, the measured and fitted XRD patterns as well as the difference between the two diffractograms are shown for the center of the disk processed by HPT for 1/4 turn and the periphery of the sample after 10 turns in Fig. 7a and b, respectively. The average diffraction domain size, dislocation density and twin fault probability obtained by XLPA are listed in Table 1. It can be seen that the diffraction domain size is about 30-40 nm for all HPT-processed samples which is much smaller than the grain sizes measured by TEM for the samples. This is a usual phenomenon in SPD-processed materials involving the hierarchical microstructure, i.e., the grains are fragmented into subgrains and dislocation cells. XLPA measures the size of these subgrains and cells. Indeed, there are large contrast differences inside the grains in the DF TEM images (an example is shown in the inset of Fig. 5h), suggesting misorientations between adjacent volumes inside the grains. The diffraction domain size decreased significantly to ~40 nm in the center of the disk processed by ½ turn. It should be noted that XLPA characterizes the microstructural parameters for the disk center with a maximum distance of about 1 mm from the actual disk center. The minimum diffraction domain size of about 30 nm was achieved in the disk processed for 1 turn by HPT. In practice, the consistent values of the minimum domain size were achieved both in the centers and peripheries of the disks after processing for 10 and 20

The dislocation density increased to about $35 \times 10^{14} \, m^{-2}$ in the center of the disk processed for ½ turn despite the moderate strain value, and it reached further to $\sim \! 120 \times 10^{14} \, m^{-2}$ at the periphery. After 1 turn of HPT, the dislocation density increased to about $80 \times 10^{14} \, m^{-2}$ in the disk center while at the periphery it reached the saturation value of $\sim \! 150 \times 10^{14} \, m^{-2}$ in the HPT-processed CoCrFeNi HEA. After 10 and 20 turns, the similar values were measured at both the centers and the peripheries of the disks.

The twin fault probability in the disk center processed by $\frac{1}{4}$ turn was zero as measured by XLPA as shown in Table 1. This result is not in

contradiction with the significant amount of twin boundaries observed in Fig. 3. The lower detection limit of twin fault probability is \sim 0.1% in XLPA which corresponds to a maximum detectable twin fault spacing of ~300 nm [25]. In the EBSD image of Fig. 3, the lowest twin boundary spacing is about 1 µm which cannot be detected by XLPA. The twin fault probability increased to about 3% at the periphery of the disk processed by 1/4 turn which can be regarded as the saturation value of this quantity in the HPT-processed CoCrFeNi HEA, i.e., there is no further increase at the periphery with increasing numbers of turns. After 1 turn of HPT, the twin fault probability in the disk center increased to \sim 2%. For 10 and 20 turns, the twin density tends to be consistent with the saturated value of about 3% throughout the disk diameter. This saturation value of the twin fault probability corresponds to an average twin fault spacing of about 7 nm. The significant twinning in the HPT-processed CoCrFeNi HEA is also confirmed by the HRTEM image in Fig. 8a and its fast Fourier transform (FFT) in Fig. 8b taken at the periphery of the sample after 10 turns. In Fig. 8b, the indices of the spots corresponding to the parent and twinned crystals located at the bottom of Fig. 8a are indicated by different colors.

It should be noted that the large relative intensity of reflection 111 in the diffractogram shown in Fig. 7 suggests the development of texture of the CoCrFeNi HEA during HPT processing. Fig. 9 shows the texture development by the 111 pole figures for (a) an initial state, (b) 1/4, (c) 1, (d) 10 and (e) 20 HPT turns, where the pole figures were obtained on the whole disks. Due to the severe deformation during HPT, it is expected that all active dislocation slip systems are populated equally by dislocations despite the texture, therefore the average contrast factors can be used in the CMWP method. The only effect of texture on the results obtained by the CMWP fitting may be the higher weight of reflection 111 compared to other peaks in the diffractograms. Therefore, the fitting procedure was repeated on modified diffractograms where the intensity of reflection 111 was reduced with a factor varying between 2 and 4 by maintaining other peaks unchanged. The

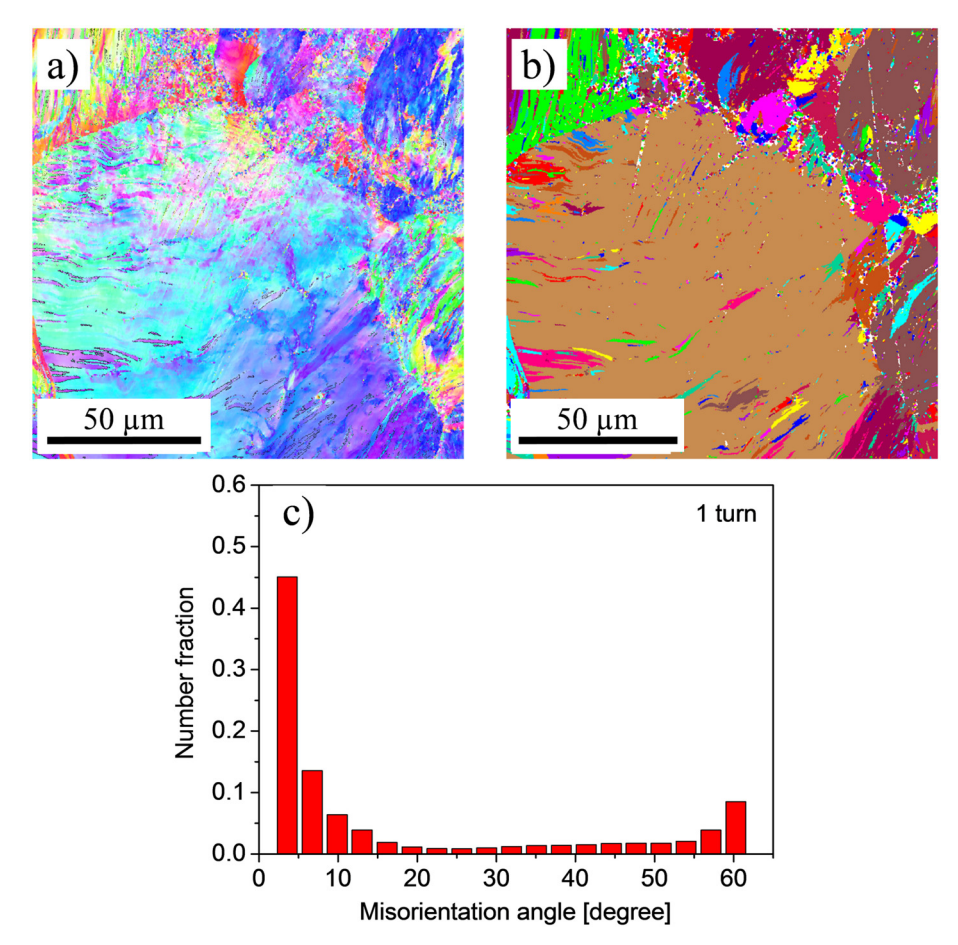


Fig. 4. Orientation (a) and grain (b) maps as well as the misorientation angle distribution (c) for the CoCrFeNi HEA processed by 1 turn of HPT.

largest factor corresponds to a 111/200 peak intensity ratio of about 2–3, depending on the sample and the location (center or periphery). No considerable difference between the results obtained by CMWP on these modified diffraction patterns was found.

3.3. Hardness evolution in the HPT-processed disks

Fig. 10 shows the variation of hardness as a function of the distance from the disk center for the HEA after the different numbers of HPT turns. The hardness of the initial CoCrFeNi HEA was 1380 $\,\pm\,$ 100 MPa. After ¼ turn, the hardness increased to $\sim\!$ 2500 and $\sim\!$ 4900 MPa in the

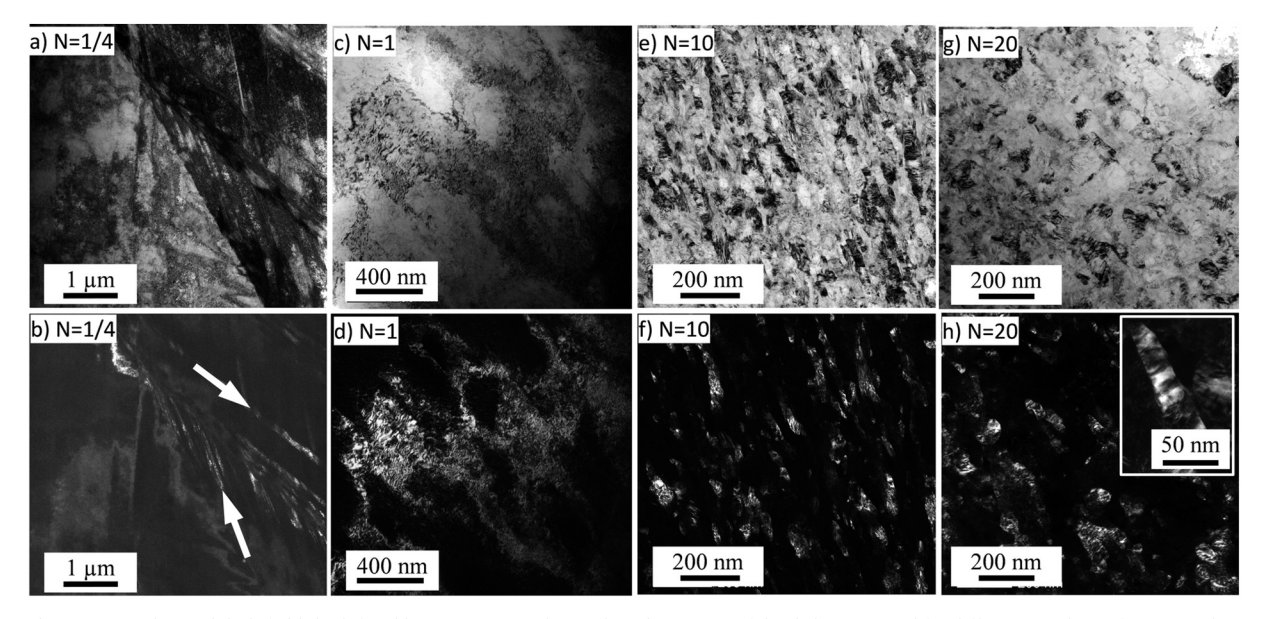


Fig. 5. Bright- (a, c, e and g) and dark-field (b, d, f and h) TEM images obtained on the centers of the disks processed for different numbers of turns. In (b) some twins are indicated by white arrows. The inset of (h) shows a grain with a higher magnification which exhibits contrast differences in DF TEM image.

Table 1
The diffraction domain size, the dislocation density and the twin fault probability determined by XLPA, as well as the grain size obtained by electron microscopy (EBSD and TEM). The corresponding shear strain values (γ) are also shown. The calculation details of the shear strain are given in the last paragraph of Section 4.1.

HPT turn/location	γ	Diffraction domain size (XLPA) [nm]	Dislocation density (XLPA) [10 ¹⁴ m ⁻²]	Twin fault probability (XLPA) [%]	Grain size (EBSD/TEM) [nm]
Initial	0	n.a.	n.a.	n.a.	22,000 ± 1000
1/4, center	1.1	38 ± 4	35 ± 4	0.0 ± 0.1	1400 ± 300
1/4, periphery	9	39 ± 4	122 ± 20	3.0 ± 0.5	91 ± 10
1, center	4.5	25 ± 3	80 ± 10	2.0 ± 0.4	860 ± 200
1, periphery	36	30 ± 5	150 ± 20	3.1 ± 0.3	61 ± 10
10, center	45	29 ± 3	141 ± 20	2.6 ± 0.6	81 ± 10
10, periphery	359	28 ± 3	140 ± 20	3.1 ± 0.3	77 ± 10
20, center	90	32 ± 5	156 ± 20	2.8 ± 0.4	90 ± 20
20, periphery	718	28 ± 3	150 ± 20	2.6 ± 0.4	79 ± 10

center and the periphery of the disk, respectively. Further increase of the numbers of HPT turns to one yielded an enhancement of the hardness to about 3800 MPa in the disk center while at the periphery only a negligible increase to \sim 5000 MPa was observed. After 10 and 20 turns, the hardness distribution was homogeneous along the disk diameter with the hardness value of 5100 \pm 300 MPa.

4. Discussion

4.1. Evolution of microstructure and hardness with increasing shear strain by HPT

Fig. 11a, b and c shows the evolution of the grain size, dislocation density and twin fault probability as a function of the nominal shear strain γ imposed during HPT-processing. The value of γ was obtained as $\gamma = 2\pi r N/h$, where r, N and h are the distance from the disk center, the number of turns and the thickness of the disk, respectively. Due to the extension of the X-ray beam used for XLPA, the parameters of the microstructure (i.e., the dislocation density and the twin fault probability) determined nominally for the disk center were related to the shear strain at r = 0.5 mm. At the same time, the grain size was determined in the center of the samples where the nominal shear strain was zero. For the microstructural parameters determined at the periphery, the shear strain was calculated using the value of r = 4 mm. The insets in Fig. 11 magnify the evolution of the microstructural parameters and the hardness at low shear strain. As shown in Fig. 11a and c, the grain size and the twin fault probability were saturated with the values of ~80 nm and 3%, respectively, at a shear strain of about 10. It is worth noting

that the saturation grain size measured in this study was in good agreement with the value determined for a HEA with the same composition and processed by 4 turns of HPT at RT (~70 nm [26]). In both this study and the former investigation, the grain sizes were measured directly from the TEM images as the diameters of the individual grains. It should also be noted that the shear strain in the center (r = 0) certainly deviates from zero due to the plasticity induced by the stress field of dislocations formed at $r \neq 0$. This induced plastic shear strain led to the significant grain refinement in the centers as shown in Table 1. Therefore, the data obtained in the centers are not considered when the evolution of the grain size is evaluated as a function of shear strain. At the strain corresponding to the saturation of grain size ($\gamma = 10$), the dislocation density reached a value of about $\sim 120 \times 10^{14} \, \text{m}^{-2}$ which is only slightly smaller than the maximum dislocation density $(\sim 150 \times 10^{14} \,\mathrm{m}^{-2})$. The latter value was achieved between the shear strains of 10 and 35 (see Fig. 11b). The fast increase of the dislocation density with increasing strain is in accordance with a recent observation of a high dislocation density (\sim 12 \times 10¹⁴ m⁻²) in a CoCrFeNi HEA even at a strain of 0.35 [27]. Fig. 11d reveals that a significant increase in hardness appeared through the strain of about $\gamma = 10$ in line with the evolution of the grain size and the twin fault probability. At this strain, the hardness reached a value of ~5000 MPa. Further increase of the shear strain to ~20 resulted only in a slight enhancement of the hardness to about 5100 MPa in accordance with the moderate increase of the dislocation density from $\sim 120 \times 10^{14} \, \text{m}^{-2}$ to $\sim 150 \times 10^{14} \, \text{m}^{-2}$. This hardness is close to the value determined in a recent study for a CoCrFeNi HEA processed also by HPT at RT [26]. However, in the former study HPT for up to 4 turns was used for the consolidation of

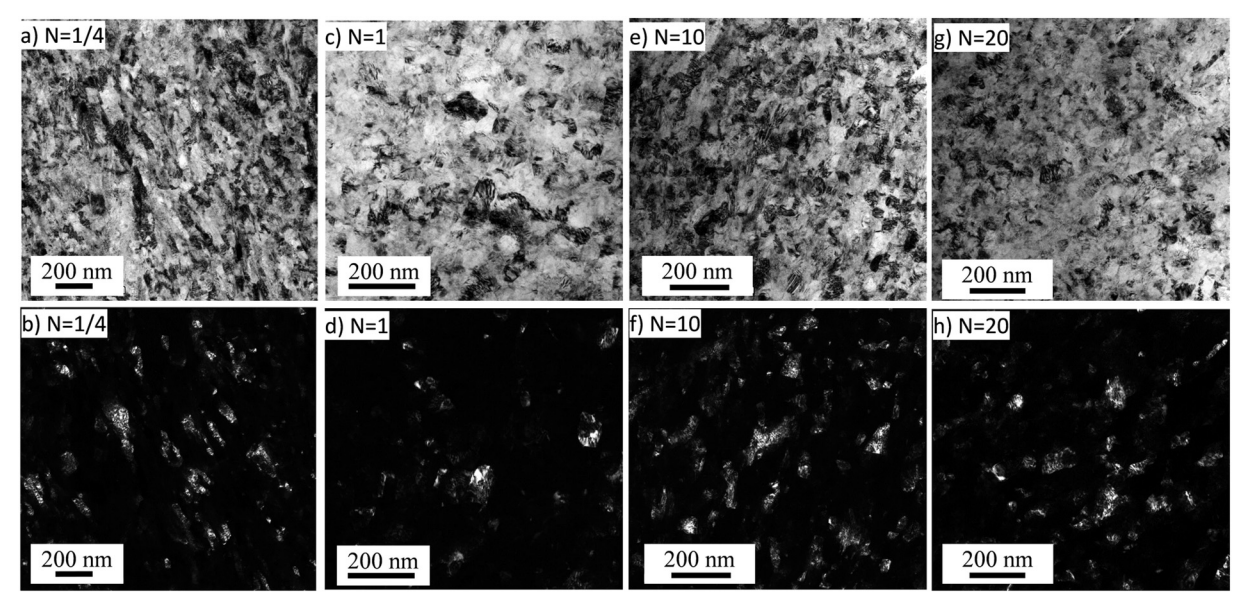
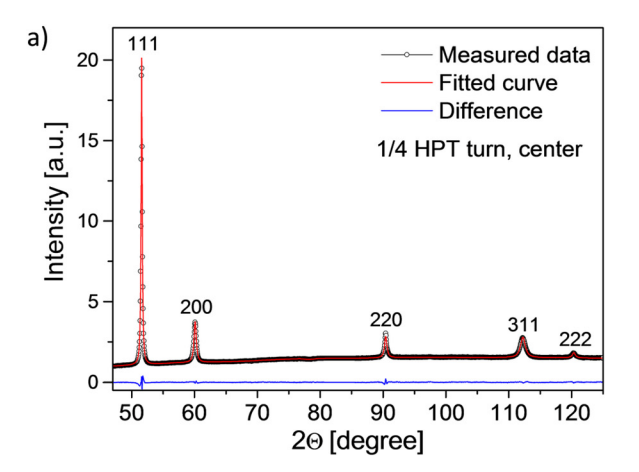


Fig. 6. Bright- (a, c, e and g) and dark-field (b, d, f and h) TEM images obtained on the peripheries of the disks processed for different numbers of turns.



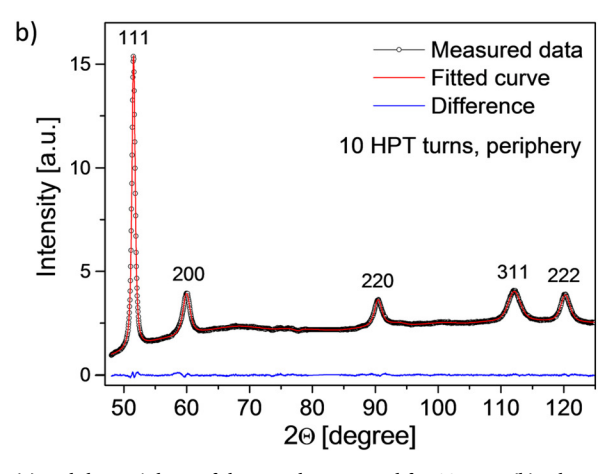


Fig. 7. CMWP fitting obtained at the center of the disk processed by HPT for ¼ turn (a) and the periphery of the sample processed for 10 turns (b). The open circles and the red solid line represent the measured and the fitted XRD patterns while the blue line at the bottom of the figure indicates the difference between them. (For interpretation of the references to colour in this figure legend, the reader is referred to the web version of this article.)

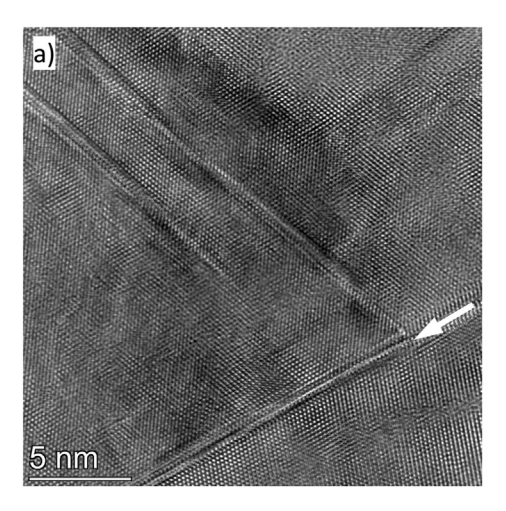
HEA powders while in the present investigation the bulk CoCrFeNi samples were processed by HPT for up to much higher numbers of turns of 20. In addition, in the former study the dislocation density was not investigated while in the present study the evolution of the dislocation density was studied in detail. In the next section, the microstructures and the hardness values obtained on the CoCrFeNi HEA is compared with the results determined formerly for the HPT-processed CoCrFeNiMn samples where such comparison is missing in the literature.

4.2. Comparison between the microstructures and hardness values observed in CoCrFeNi and CoCrFeNiMn HEAs processed by HPT

In a former study [4], we investigated the effect of HPT-processing on the microstructure and hardness of a five-component equimolar CoCrFeNiMn HEA. The material differs from the present four-component HEA as the latter one does not contain Mn. The defect structures in both HPT-processed alloys were investigated by the same XLPA methodology. The saturation dislocation density and twin fault probability determined by XLPA and the minimum achievable grain size obtained by TEM are listed in Table 2 for both HEAs. Despite the different compositions of these HEAs, the saturation twin fault probability are reasonably consistent (\sim 3%) which can be explained by the similar SFE in these two materials (\sim 20–30 mJ/m² [24,26,28]). The diffraction domain size in the quaternary alloy (28 \pm 3 nm) was also similar to the value determined for the five-component HEA (22 \pm 3 nm). The maximum dislocation density in the present CoCrFeNi HEA (150 \pm 20 \times 10¹⁴ m $^{-2}$) was slightly lower than the value determined

for the CoCrFeNiMn HEA (194 \pm 20 \times 10¹⁴ m⁻²). The saturation grain size taken by TEM was higher (\sim 80 nm) in the present CoCrFeNi HEA than the CoCrFeNiMn HEA (\sim 27 nm) processed by HPT at RT.

The difference between the saturation dislocation densities and grain sizes achieved by HPT in these two alloys can be correlated with the effect of Mn on the structure of CoCrFeNi HEA. A former study has shown that for Mn atoms in a CoCrFeNiMn HEA the bond distance with the nearest neighbors is slightly larger than between other elements [29]. This suggests a larger lattice distortion around Mn atoms in CoCrFeNiMn HEA. This distortion may be relaxed in the dilatation zone of a dislocation, resulting in an attractive interaction between Mn atoms and dislocations. Thus, the motion of dislocations is highly hindered in CoCrFeNiMn as manifested by the higher friction stress of dislocation glide at RT in CoCrFeNiMn (~200 MPa [30-32]) than in CoCrFeNi (~140 MPa [33]). In addition, it was shown that the addition of Mn to CoCrFeNi led to a more favorable formation of a Mn-Co nearestneighbour pair than Mn-Ni in the fcc structure [34]. Thus, the separation of Mn-Co pairs by dislocation motion is not favorable energetically, thereby hindering the movement of dislocations. Other researches [35,36] have revealed that the diffusion (e.g., for Ni) in CoCrFeNiMn is slower than in CoCrFeNi at RT where the slower diffusion delays the climb of dislocations despite the lower melting point of CoCrFeNiMn. Due to the above reasons, the annihilation of dislocations is impeded, resulting in a higher saturation dislocation density in the HPT-processed CoCrFeNiMn HEA. As the rearrangement of dislocations into boundaries is usually an important mechanism for grain refinement, the higher dislocation density in the HPT-processed



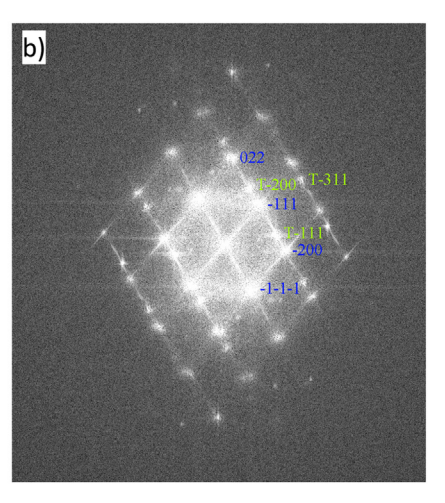


Fig. 8. HRTEM image (a) together with its FFT (b) showing twins at the periphery of the disk processed by 10 turns of HPT. The twin corresponding to the FFT is indicated by a white arrow in (a). In (b), the indices of the spots corresponding to the parent and twinned crystals are indicated by different colors. (For interpretation of the references to colour in this figure legend, the reader is referred to the web version of this article.)

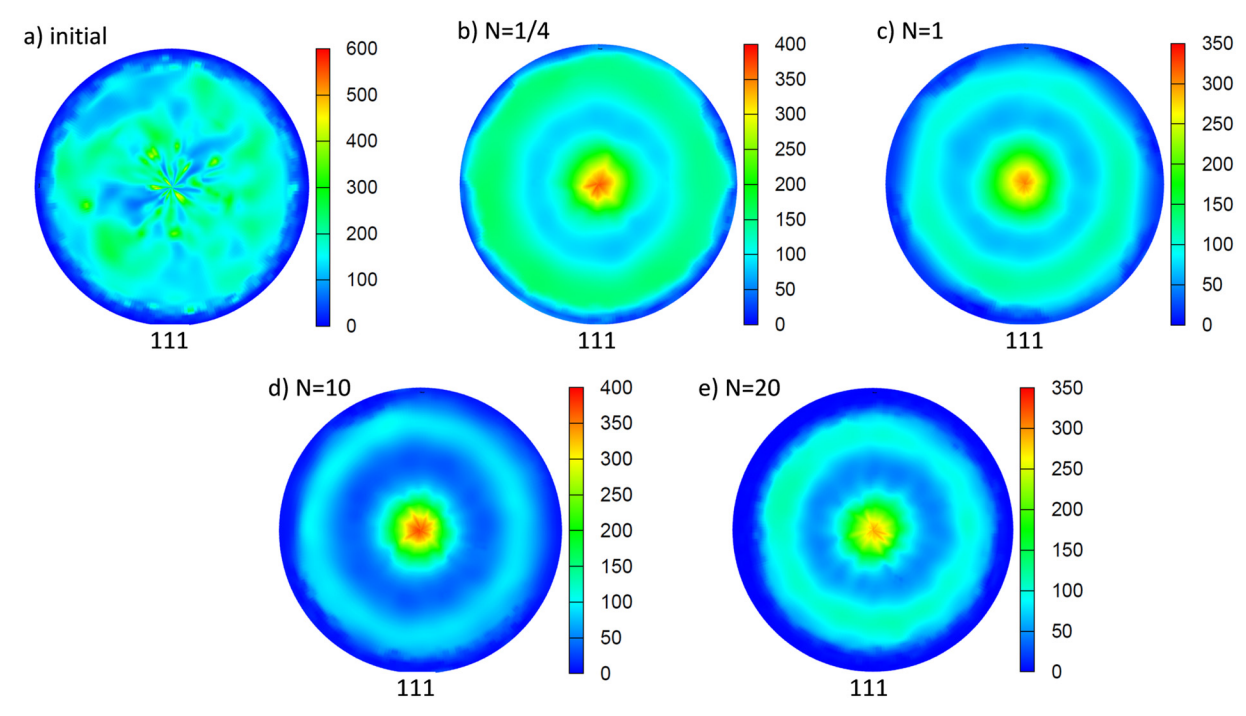


Fig. 9. 111 XRD pole figures measured on the initial sample and the disks processed by different numbers of HPT turns.

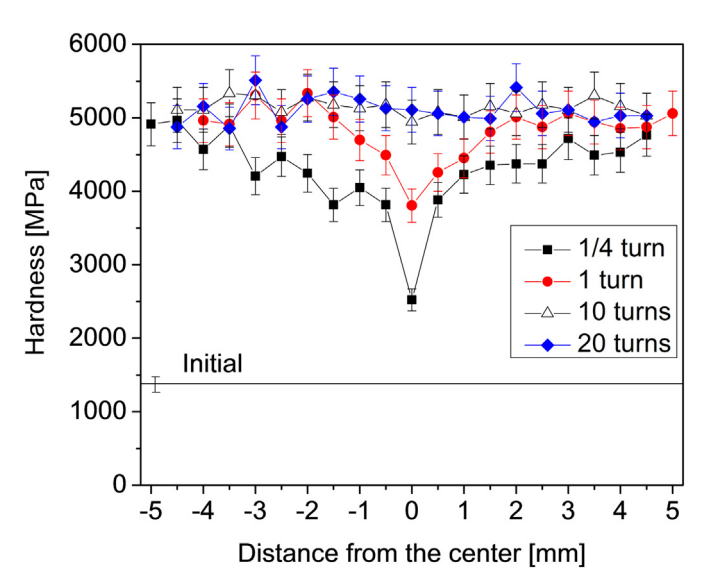


Fig. 10. The hardness versus the distance from the disk center processed by different numbers of HPT turns.

CoCrFeNiMn could cause smaller grain sizes in the HEA. It should be noted that Mn segregation at grain boundaries was not observed formerly in CoCrFeNiMn HEA and the grain boundary energies for the CoCrFeNiMn and CoCrFeNi alloys were found to be reasonably equivalent (\sim 0.65 J/m²) [36].

The evolution of the hardness versus the nominal shear strain for the HPT-processed CoCrFeNiMn and CoCrFeNi HEAs was compared in Fig. 12. As seen in Fig. 11d, the hardness saturated at a shear strain of about 10 for the present CoCrFeNi HEA, while the hardness saturation for the CoCrFeNiMn alloy was achieved at a higher strain of ~40 due to a slower increase of the twin fault probability. However, the saturation hardness values were similar as 5100–5400 MPa (see Table 2) which can be attributed to the similar defect density levels in the two alloys. Although, the minimum grain sizes were different in the CoCrFeNi and CoCrFeNiMn HEAs, the average twin fault spacing in the saturation

state (as calculated from the twin fault probability) had the consistent values (7–8 nm) for the two alloys. Former studies [37,38] have shown that twin faults have the same strengthening effect as grain boundaries. Therefore, the Hall-Petch hardening is equally effective for the CoCrFeNi and CoCrFeNiMn HEAs. The Taylor-type strengthening may also affect similarly as the saturation dislocation density is only slightly smaller in the CoCrFeNi. The small difference between the dislocation densities in the HPT-processed CoCrFeNi and CoCrFeNiMn HEAs did not cause measurable difference in the hardness due to its experimental error and the fact that the strength varies with the square-root of the dislocation density.

5. Conclusions

The CoCrFeNi HEA disks were processed by HPT at RT up to 20 turns. The microstructure and hardness were studied as a function of the shear strain. The results were compared with those determined for a CoCrFeNiMn HEA processed under the same HPT conditions. The following conclusions were obtained:

- 1. The initial grain size of $\sim\!22\,\mu m$ was refined to $\sim\!1.4\,\mu m$ in the center of the disk processed for $^{1}\!\!/4$ turn while the grain size was reduced to 90 nm at the disk periphery. Simultaneously, the dislocation density increased to $\sim\!35\times10^{14}\,m^{-2}$ and $\sim\!122\times10^{14}\,m^{-2}$ at the center and the periphery, respectively, after $^{1}\!\!/4$ turn. At the periphery of the disk, the twin fault probability reached as high as $\sim\!3\%$. After 10 turns by HPT, microstructural homogeneity was demonstrated reasonably so that a saturation was achieved with a grain size value of about 80 nm, a dislocation density of $\sim\!150\times10^{14}\,m^{-2}$ and a twin fault probability of $\sim\!3\%$ at both disk center and pheriphey. Moreover, HPT processing resulted in the development of a strong 111 texture in the HEA.
- 2. The maximum twin fault probability (\sim 3%) was consistent in both CoCrFeNi and CoCrFeNiMn HEAs due to the similar SFE (20–30 mJ/m²). However, the saturation dislocation density was lower (\sim 150 \times 10¹⁴ m $^{-2}$) and the grain size was larger (\sim 80 nm) in the present HEA of CoCrFeNi. These differences are due to the absence of the lattice distortion by Mn and the slower diffusion in

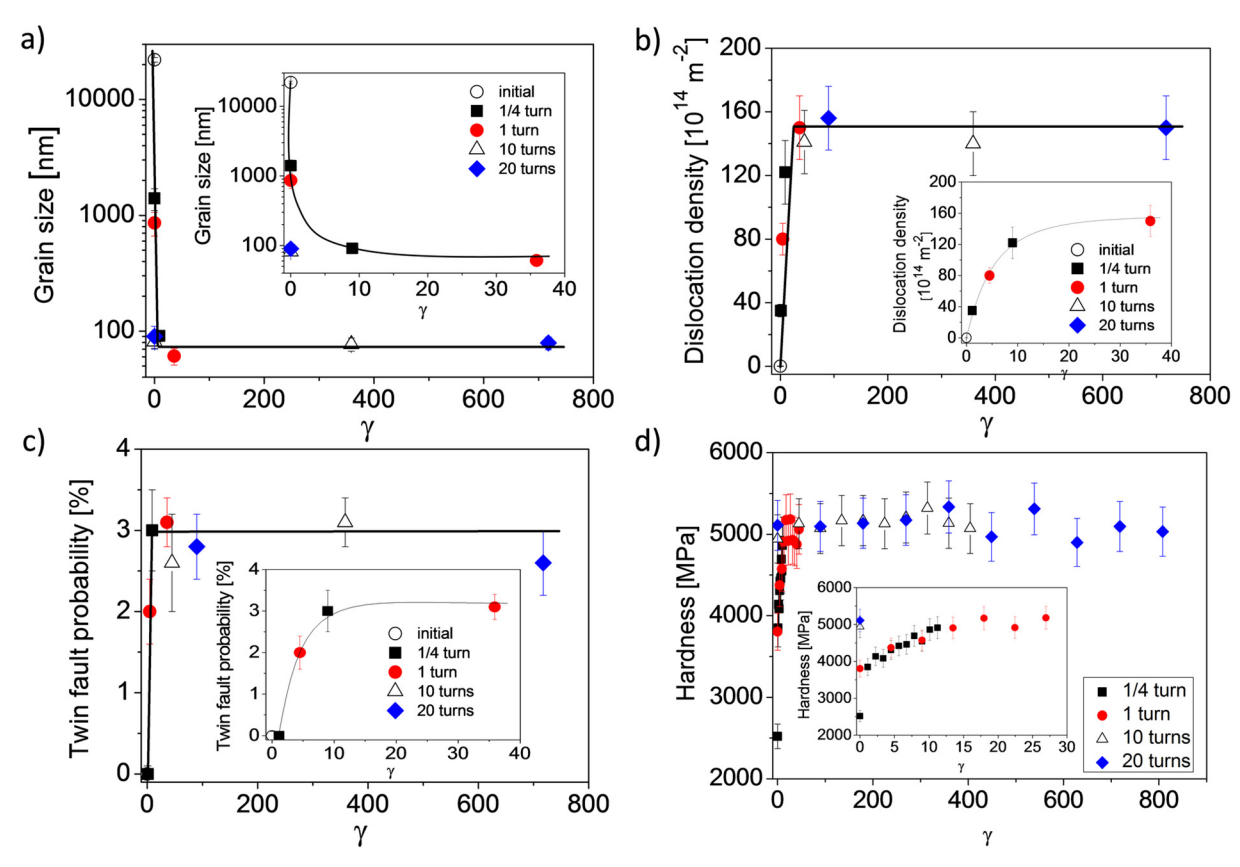


Fig. 11. Evolution of the grain size (a), dislocation density (b), twin fault probability (c) and hardness (d) obtained in the centers and the peripheries of the disks processed by different numbers of turns as a function of the nominal shear strain. The insets show the evolution of the microstructural parameters and the hardness for low strain values.

CoCrFeNiMn alloy which hinder the annihilation of dislocations and the grain boundary motion during HPT.

3. Despite the different grain sizes in the CoCrFeNi and CoCrFeNiMn HEAs, the saturation hardness values were similar as 5100–5400 MPa. This can be explained by the similar defect densities, especially if the similarly high values of the twin fault probability with the twin fault spacing (7–8 nm) are considered. The latter defects can harden the material in a same way as the general grain boundaries. The saturation hardness was observed in an early stage of straining at ~10 in the CoCrFeNi HEA while it is at ~40 in the CoCrFeNiMn alloy due to the Mn addition delaying the evolution of twin faulting.

Data availability

The raw/processed data required to reproduce these findings cannot be shared at this time due to technical or time limitations.

Declaration of Competing Interest

The authors declare that they have no conflict of interest.

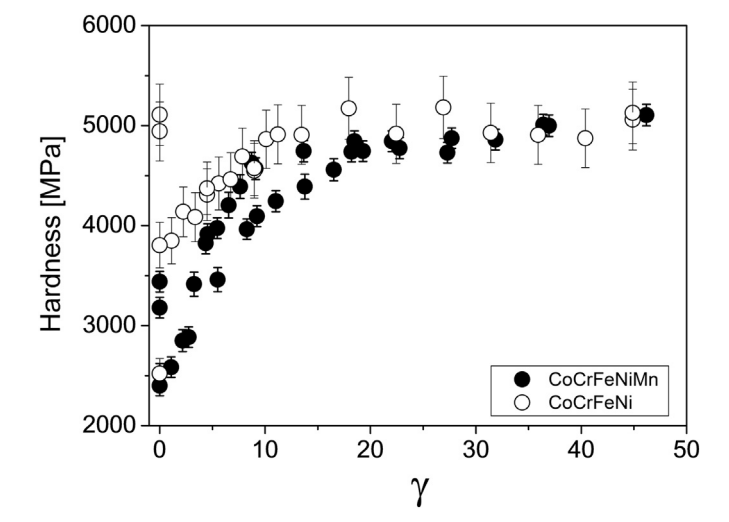


Fig. 12. Comparison of the evolution of the hardness as a function of the nominal shear strain for CoCrFeNi and CoCrFeNiMn HEAs processed by HPT.

Table 2 Comparison of the saturation dislocation density and twin fault probability determined by XLPA, the saturation grain size obtained by TEM and the saturation hardness determined for CoCrFeNi and CoCrFeNiMn HEAs processed by HPT at RT. In addition to the grain size, the saturation twin boundary (TB) spacing is also shown in parentheses.

Composition	Dislocation density [10 ¹⁴ m ⁻²]	Twin fault probability [%]	Grain size (TB spacing) [nm]	Hardness [MPa]	Reference
CoCrFeNi	150 ± 20 194 ± 20	3.0 ± 0.5	$80 \pm 10 (7 \pm 1)$	5100 ± 300	[This study]
CoCrFeMnNi		2.7 ± 0.2	$27 \pm 5 (8 \pm 1)$	5380 ± 100	[4]

Acknowledgement

This work was supported in part by the Ministry of Human Capacities of Hungary within the ELTE University Excellence program (1783-3/2018/FEKUTSRAT); in part by the grant no. VEKOP-2.3.3-15-2016-00002 of the European Structural and Investment Funds; and in part by the National Science Foundation of the United States under Grant No. DMR-1810343. The preparation of the TEM lamellae by Andrea Fenyvesi-Jakab is also acknowledged.

References

- [1] J.-W. Yeh, S.-K. Chen, S.-J. Lin, J.-Y. Gan, T.-S. Chin, T.-T. Shun, C.-H. Tsau, S.-Y. Chang, Nanostructured high-entropy alloys with multiple principal elements: novel alloy design concepts and outcomes. Adv. Eng. Mater. 6 (2004) 299–303.
- [2] Y. Ikeda, B. Grabowski, F. Körmann, Ab initio phase stabilities and mechanical properties of multicomponent alloys: a comprehensive review for high entropy alloys and compositionally complex alloys, Mater. Charact. 147 (2019) 464–511.
- [3] Y. Zhang, T.T. Zuo, Z. Tang, M.C. Gao, K.A. Dahmen, P.K. Liaw, Z.P. Lu, Microstructures and properties of high-entropy alloys, Prog. Mater. Sci. 61 (2014) 1–93.
- [4] A. Heczel, M. Kawasaki, J.L. Lábár, J. Jang, T.G. Langdon, J. Gubicza, Defect structure and hardness in nanocrystalline CoCrFeMnNi high-entropy alloy processed by high-pressure torsion, J. Alloys Compd. 711 (2017) 143–154.
- [5] H. Yuan, M. Tsai, G. Sha, F. Liu, Z. Horita, Y. Zhu, J.T. Wang, Atomic-scale homogenization in an fcc-based high-entropy alloy via severe plastic deformation, J. Alloys Compd. 686 (2016) 15–23.
- [6] E. Pickering, R. Muñoz-Moreno, H.J. Stone, N.G. Jones, Precipitation in the equiatomic high-entropy alloy CrMnFeCoNi, Scr. Mater. 113 (2016) 106–109.
- [7] M. Vaidya, G.M. Muralikrishna, S. Divinski, B. Murty, Experimental assessment of the thermodynamic factor for diffusion in CoCrFeNi and CoCrFeMnNi high entropy alloys, Scr. Mater. 157 (2018) 81–85.
- [8] W. Huo, H. Zhou, F. Fang, X. Hu, Z. Xie, J. Jiang, Strain-rate effect upon the tensile behavior of CoCrFeNi high-entropy alloys, Mater. Sci. Eng. A 689 (2017) 366–369.
- [9] A. Verma, P. Tarate, A. Abhyankar, M. Mohape, D. Gowtam, V. Deshmukh, T. Shanmugasundaram, High temperature wear in CoCrFeNiCuX high entropy alloys: the role of Cu, Scr. Mater. 161 (2019) 28–31.
- [10] G. Sathiaraj, M. Ahmed, P.P. Bhattacharjee, Microstructure and texture of heavily cold-rolled and annealed fcc equiatomic medium to high entropy alloys, J. Alloys Compd. 664 (2016) 109–119.
- [11] W. Huo, F. Fang, H. Zhou, Z. Xie, J. Shang, J. Jiang, Remarkable strength of CoCrFeNi high-entropy alloy wires at cryogenic and elevated temperatures, Scr. Mater. 141 (2017) 125–128.
- [12] W. Huo, X. Liu, S. Tan, F. Fang, Z. Xie, J. Shang, J. Jiang, Ultrahigh hardness and high electrical resistivity in nano-twinned, nanocrystalline high-entropy alloy films, Appl. Surf. Sci. 439 (2018) 222–225.
- [13] J. Li, W. Jia, J. Wang, H. Kou, D. Zhang, E. Beaugnon, Enhanced mechanical properties of a CoCrFeNi high entropy alloy by supercooling method, Mater. Des. 95 (2016) 183–187.
- [14] T. Lindner, M. Löbel, B. Sattler, T. Lampke, Surface hardening of fcc phase high-entropy alloy system by powder-pack boriding, Surf. Coat. Technol. (2019), https://doi.org/10.1016/j.surfcoat.2018.10.017.
- [15] S. Praveen, J. Basu, S. Kashyap, R.S. Kottada, Exceptional resistance to grain growth in nanocrystalline CoCrFeNi high entropy alloy at high homologous temperatures, J. Alloys Compd. 662 (2016) 361–367.
- [16] J. Wang, T. Guo, J. Li, W. Jia, H. Kou, Microstructure and mechanical properties of non-equilibrium solidified CoCrFeNi high entropy alloy, Mater. Chem. Phys. 210 (2018) 192–196.

- [17] A.P. Zhilyaev, T.G. Langdon, Using high-pressure torsion for metal processing: fundamentals and applications, Prog. Mater. Sci. 53 (2008) 893–979.
- [18] Q. Tang, Y. Huang, Y. Huang, X. Liao, T.G. Langdon, P. Dai, Hardening of an Al_{0.3}CoCrFeNi high entropy alloy via high-pressure torsion and thermal annealing, Mater. Lett. 151 (2015) 126–129.
- [19] R.B. Figueiredo, P.R. Cetlin, T.G. Langdon, Using finite element modeling to examine the flow processes in quasi-constrained high-pressure torsion, Mater. Sci. Eng. A 528 (2011) 8198–8204.
- [20] D.P. Nelson, J.B. Riley, An experimental investigation of extrapolation methods in the derivation of accurate unit-cell dimensions of crystals, Proc. Phys. Soc. 57 (1945) 160–177.
- [21] G. Ribárik, J. Gubicza, T. Ungár, Correlation between strength and microstructure of ball-milled Al-Mg alloys determined by X-ray diffraction, Mater. Sci. Eng. A 387-389 (2004) 343–347.
- [22] A. Borbély, J. Dragomir-Cernatescu, G. Ribárik, T. Ungár, Computer program ANIZC for the calculation of diffraction contrast factors of dislocations in elastically anisotropic cubic, hexagonal and trigonal crystals, J. Appl. Crystallogr. 36 (2003) 160–162
- [23] F. Tian, L.K. Varga, J. Shen, L. Vitos, Calculating elastic constants in high-entropy alloys using the coherent potential approximation: current issues and errors, Comput. Mater. Sci. 111 (2016) 350–358.
- [24] A.J. Zaddach, C. Niu, C.C. Koch, D.L. Irving, Mechanical properties and stacking fault energies of NiFeCrCoMn high-entropy alloy, JOM 65 (2013) 1780–1789.
- [25] J. Gubicza, X-ray Line Profile Analysis in Materials Science, IGI-Global, Hershey, PA, 2014.
- [26] W. Wu, M. Song, S. Ni, J. Wang, Y. Liu, B. Liu, X. Liao, Dual mechanisms of grain refinement in a FeCoCrNi high entropy alloy processed by high pressure torsion, Sci. Rep. 7 (2017) 46720.
- [27] B. Wang, H. He, M. Naeem, S. Lan, S. Harjo, T. Kawasaki, Y. Nie, H.W. Kui, T. Ungár, D. Ma, A.D. Stoica, Q. Li, Y. Ke, C.T. Liu, X.L. Wang, Deformation of CoCrFeNi high entropy alloy at large strain, Scr. Mater. 155 (2018) 54–57.
- [28] M. Beyramali Kivy, M. Asle Zaeem, Generalized stacking fault energies, ductilities, and twinnabilities of CoCrFeNi-based face-centered cubic high entropy alloys, Scr. Mater. 139 (2017) 83–86.
- [29] F. Zhang, Y. Tong, K. Jin, H. Bei, W.J. Weber, A. Huq, A. Lanzirotti, M. Newville, D.C. Pagan, J.Y.P. Ko, Y. Zhang, Chemical complexity induced local structural distortion in NiCoFeMnCr high-entropy alloy, Mater. Res. Lett. 6 (2018) 450–455.
- [30] A. Gali, E.P. George, Tensile properties of high- and medium-entropy alloys, Intermetallics 39 (2013) 74–78.
- [31] F. Otto, A. Dlouhy, C. Somsen, H. Bei, G. Eggeler, E.P. George, The influences of temperature and microstructure on the tensile properties of a CoCrFeMnNi highentropy alloy, Acta Mater. 61 (2013) 5743–5755.
- [32] B. Gludovatz, E.P. George, R.O. Ritchie, Processing, microstructure and mechanical properties of the CrMnFeCoNi, JOM 67 (10) (2015) 2262–2270.
- [33] G.A. Salishchev, M.A. Tikhonovsky, D.G. Shaysultanov, N.D. Stepanov, A.V. Kuznetsov, I.V. Kolodiy, A.S. Tortika, O.N. Senkov, Effect of Mn and V on structure and mechanical properties of high-entropy alloys based on CoCrFeNi system, J. Alloys Compd. 591 (2014) 11–21.
- [34] M.A. Gutierrez, G.D. Rodriguez, G. Bozzolo, H.O. Mosca, Melting temperature of CoCrFeNiMn high-entropy alloys, Comput. Mater. Sci. 148 (2018) 69–75.
- [35] M. Vaidya, S. Trubel, B.S. Murty, G. Wilde, S.V. Divinski, Ni tracer diffusion in CoCrFeNi and CoCrFeMnNi high entropy alloys, J. Alloys Compd. 688 (2016) 994–1001
- [36] M. Vaidya, K.G. Pradeep, B.S. Murty, G. Wilde, S.V. Divinski, Radioactive isotopes reveal a non sluggish kinetics of grain boundary diffusion in high entropy alloys, Sci. Rep. 7 (2017) 12293.
- [37] B.B. Rath, M.A. Imam, C.S. Pande, Nucleation and growth of twin interfaces in fcc metals and alloys, Mater. Chem. Phys. 1 (2000) 61–66.
- [38] K. Lu, L. Lu, S. Suresh, Strengthening materials by engineering coherent internal boundaries at the nanoscale, Science 324 (2009) 349–352.